

Surface Plasmon Polaritons in a Waveguide Composed of Weyl Semimetals with Different Symmetries

S. Oskoui Abdol, B. Abdollahipour*, A. Soltani Vala

Department of condensed matter physics, Faculty of Physics, University of Tabriz, Tabriz 51666-16471, Iran

(Dated: April 6, 2020)

The peculiar topological properties of Weyl semimetals lead to unusual and unique optical properties. We investigate novel features of surface plasmon polaritons in a slot waveguide comprised of two semi-infinite Weyl semimetals with different symmetries, one with broken time reversal symmetry and the other one with broken inversion symmetry. We consider Voigt and Faraday configurations for surface plasmon polaritons at the interface of the Weyl semimetal with broken time reversal symmetry. We demonstrate that in the Voigt configuration this structure supports unidirectional surface plasmon polariton modes above the bulk plasmon frequency while it shows a nonreciprocal bidirectional dispersion for surface plasmon polaritons below the bulk plasmon frequency. In particular, we show that the chiral nature of the surface plasmon polaritons can be tuned by the topological properties and chemical potential of the Weyl semimetals. Moreover, in the Faraday configuration we find a tunable gap in the surface plasmon polariton dispersion. The studied structures possessing these exotic features may be employed as one of the building blocks of the chiral optoelectronic devices.

PACS numbers: 73.20.Mf, 78.68.+m, 42.79.Gn, 03.65.Vf

I. INTRODUCTION

Weyl semimetals (WSMs) have recently attracted intensive attention due to their exotic band structure¹. The anomalous band structure of WSMs manifests itself in their topological properties such as protected Weyl nodes and Fermi arc surface states^{2,3}. The conduction and valance bands in WSMs touch each other at Weyl nodes characterized by linear dispersion around the Fermi level⁴. The Weyl nodes appear in pair with different chiralities separated in momentum or energy space in WSMs with broken time reversal symmetry (TRS)⁵ or spatial inversion symmetry (SIS)⁶, respectively. Weyl semimetal phase has been observed in topologically nontrivial materials including the nonmagnetic samples such as, TaAs⁷, NbAs⁸, NbP⁹ and magnetic compounds $Y_2Ir_2O_7$ ¹⁰ and $Eu_2Ir_2O_7$ ¹¹. Moreover, the so called type-II Weyl semimetal phase has been observed recently in materials such as WTe_2 ¹² and $MoTe_2$ ¹³ having open Fermi surfaces. Some exotic effects such as chiral anomaly¹⁴, anomalous Hall effect^{15,16} and negative magnetoresistance¹⁷ arise from the non-trivial topological band structure of WSMs. In particular, an unusual optical response emerges in WSMs due to the coupling of the electrical and magnetical properties originating from the chiral anomaly¹⁸⁻²³.

The WSMs are promising materials for photonics and plasmonics applications due to broad tunability of their chemical potential. Surface plasmon polaritons (SPPs) at the surface of WSMs have been studied theoretically²⁴⁻²⁹ and have been observed at visible wavelengths in WTe_2 ³⁰. SPPs are collective electromag-

netic and electronic charge excitations confined to the interface of a conductor with a dielectric³¹. SPPs are employed in the optoelectronic devices such as surface plasmon resonance sensor³² and scanning near field optical microscopy³³. It has been shown that an unconventional plasmon mode exist in WSMs due to the chiral anomaly which can be used as a signature of the Weyl semimetal phase²⁴. The interface of two adjacent WSMs with different magnetization orientations hosts a low-loss localized guided SPPs²⁵. It has been demonstrated that the SPP dispersion depends on the Weyl nodes separation in energy or momentum space²⁶. In a WSM with broken TRS the Weyl nodes separation vector acts as an effective external magnetic field. Furthermore, it has been predicted that a giant nonreciprocal waveguide electromagnetic modes exist in WSM thin films in the Voigt configuration²⁷. The thickness of WSM thin film and dielectric contrast of the outer insulators can be used to fine-tuning of the SPP dispersion and its nonreciprocal property²⁸. Recently, we have studied the SPP dispersion and its properties in a WSM waveguide comprised of two TRS WSMs in different configurations²⁹. In particular, it has been shown that a tremendous unidirectional SPP modes are hosted by this structure and can be tuned by the chemical potential and topological parameters of the WSMs. It is worth to note that these intriguing features of SPP modes in WSMs emerge without need to application of high external magnetic fields. On the other hand, SPP modes on the surface of topological insulators (TIs)^{34,35}, exhibiting a bulk gap and gapless surface states protected by TRS, as the first member of the family of topological materials have been investigated theoretically³⁶⁻⁴⁰ and experimentally^{41,42}. Due to identical linear Dirac electronic dispersion of the surface states in TI and graphene, these materials exhibit very similar dispersion for SPP modes. But, the spin-

*Corresponding author: b-abdollahi@tabrizu.ac.ir

momentum locking in the TIs gives rise to the charge and spin density waves leading to the spin-coupled surface plasmons or spin plasmons^{36,37}. Moreover, exciting magneto-optical Kerr effect in TIs by employing a ferromagnetic coupling or an external magnetic field results in generation of a novel transverse SPP modes in addition to the usual longitudinal one^{38–40}.

In this paper we study the interplay of the SPP modes exist at the interfaces of two WSMs with broken TRS and SIS connected via a dielectric layer in the slot waveguide geometry. We consider both Voigt and Faraday configurations for SPP propagation at the interface of the WSM with broken TRS. We demonstrate that interplay of the SPP modes localized at independent interfaces of two WSMs with different symmetries leads to unidirectional SPP modes in the waveguide geometry for the frequencies above the bulk plasmon frequency. However, we find a nonreciprocal bidirectional dispersion for SPP modes with frequencies below the bulk plasmon frequency. In particular, our analysis reveals that these chiral SPP modes can be tuned by the topological parameters and chemical potentials of two WSMs. In addition, we observe a gapful SPP dispersion in the Faraday configuration. We show that the gap of the dispersion can be controlled by the physical parameters of the WSMs. These exotic features originating from intrinsic topological properties of WSMs may be employed practically in optical devices.

The remainder of the paper is organized as follows: In Section II we introduce our theoretical model and give necessary equations for deriving SPP dispersion. Section III is devoted to presenting results and related discussions. Finally, we end by giving conclusion in Section IV.

II. THEORETICAL MODEL AND EQUATIONS

The unique optical response of a WSM originating from the intrinsic topological nature of it, is characterized by a term $\theta(\mathbf{r}, t) = 2(\mathbf{b} \cdot \mathbf{r} - b_0 t)$ which is called *axion angle*²⁰. Here \mathbf{b} expresses the vector connecting two Weyl points in momentum space of a WSM with broken TRS, whereas b_0 is the separation of them in energy for a WSM with broken SIS. The topological properties of WSMs result in a modified displacement electric field given by²⁶,

$$D = (\varepsilon_\infty + \frac{4\pi i}{\omega} \sigma) \mathbf{E} + \frac{ie^2}{\pi \hbar \omega} (\nabla \theta) \times \mathbf{E} + \frac{ie^2}{\pi \hbar c \omega} \dot{\theta} \mathbf{B}, \quad (2.1)$$

where \mathbf{E} , \mathbf{B} , ε_∞ and σ are the electric field, the magnetic field, the static dielectric constant and the conductivity of WSM, respectively. The second and third terms of Eq. 2.1 originate from the topological properties of WSM corresponding to the anomalous Hall effect and the chiral magnetic effect, respectively¹. Whereas, the first term of this equation is the usual displacement field for a normal metal.

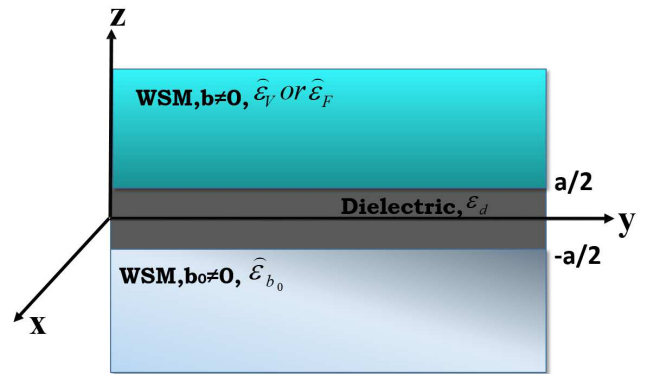


FIG. 1: Schematic of the slot waveguide constructed of two semi-infinite WSMs connected by a dielectric layer with thickness a and dielectric constant ε_d .

For a WSM with broken TRS ($\mathbf{b} \neq 0$), the chiral anomaly cause to anisotropic optical response characterized by a dielectric tensor $\hat{\varepsilon}(\omega)$, with diagonal and off diagonal terms which we will denote them by $\varepsilon(\omega)$ and $\varepsilon_b(\omega)$, respectively. Also, a WSM with broken SIS ($b_0 \neq 0$) represents anisotropic optical response with the same diagonal terms but having different off diagonal terms represented by $\varepsilon_{b_0}(\omega)$.

The SPP localized at the interface of a WSM with a dielectric is described by an electric field of the form,

$$\mathbf{E} = (E_x, E_y, E_z) e^{i\mathbf{q} \cdot \mathbf{r}_\perp} e^{-\kappa|z|} e^{-i\omega t}, \quad (2.2)$$

which decays exponentially away from the interface in the z direction and propagates in the interface along the direction of $\mathbf{q} = (q_x, q_y, 0)$. This electric field should be satisfied by the wave equation,

$$\nabla \times (\nabla \times \mathbf{E}) = -\frac{1}{c^2} \frac{\partial^2 \mathbf{D}}{\partial t^2}. \quad (2.3)$$

This equation can be expressed as a matrix equation $\hat{M}\mathbf{E} = 0$, with \hat{M} given by,

$$\hat{M} = \begin{pmatrix} q_y^2 - \kappa^2 & -q_x q_y & \mp i q_x \kappa \\ -q_x q_y & q_x^2 - \kappa^2 & \mp i q_y \kappa \\ \mp i q_x \kappa & \mp i q_y \kappa & q_x^2 + q_y^2 \end{pmatrix} - \frac{\omega^2}{c^2} \hat{\varepsilon}(\omega), \quad (2.4)$$

with the positive sign for $z < 0$ and negative one for $z > 0$. The decay constant (κ) is determined by the condition $\det(\hat{M}) = 0$. The decay constant in the WSM side depends on the relative direction of the vectors \mathbf{q} and \mathbf{b} .

The system under consideration is a slot waveguide depicted in Fig. 1. The slot waveguide has been constructed of two semi-infinite WSMs, media **I** and **III** in the figure, connected by a dielectric layer (medium **II**) with thickness a and a dielectric constant ε_d .

We consider TRS is broken in the upper WSM (medium **I**) while in the lower one (medium **III**) SIS

is broken. Relative direction of the vectors \mathbf{b} and \mathbf{q} results in different configurations for SPP propagation. We study two different Voigt and Faraday configurations at the upper interface. In the Voigt configuration \mathbf{b} is parallel to the surface but perpendicular to \mathbf{q} . By considering $\mathbf{q} = (0, q, 0)$ and $\mathbf{b} = (b, 0, 0)$ matrix \hat{M} is expressed as,

$$\hat{M}_V = \begin{pmatrix} q^2 - \kappa_1^2 & 0 & 0 \\ 0 & -\kappa_1^2 & -iq\kappa_1 \\ 0 & -iq\kappa_1 & q^2 \end{pmatrix} - k_0^2 \hat{\varepsilon}_V(\omega), \quad (2.5)$$

with

$$\hat{\varepsilon}_V(\omega) = \begin{pmatrix} \varepsilon & 0 & 0 \\ 0 & \varepsilon & i\varepsilon_b \\ 0 & -i\varepsilon_b & \varepsilon \end{pmatrix}. \quad (2.6)$$

In the Faraday configuration $\mathbf{b} = (0, b, 0)$ is parallel to the interface and $\mathbf{q} = (0, q, 0)$. In this case the matrix \hat{M} is given by,

$$\hat{M}_F = \begin{pmatrix} q^2 - \kappa_1^2 & 0 & 0 \\ 0 & -\kappa_1^2 & -iq\kappa_1 \\ 0 & -iq\kappa_1 & q^2 \end{pmatrix} - k_0^2 \hat{\varepsilon}_F(\omega), \quad (2.7)$$

with

$$\hat{\varepsilon}_F(\omega) = \begin{pmatrix} \varepsilon & 0 & i\varepsilon_b \\ 0 & \varepsilon & 0 \\ -i\varepsilon_b & 0 & \varepsilon \end{pmatrix}. \quad (2.8)$$

Since the lower WSM (medium **III**) is assumed to be SIS broke ($\mathbf{b} = 0, b_0 \neq 0$), thus off diagonal terms of the dielectric tensor results from the third term of Eq. (2.1). In this case the matrix \hat{M} can be written in the following form,

$$\hat{M}_{b_0} = \begin{pmatrix} q^2 - \kappa_3^2 & 0 & 0 \\ 0 & -\kappa_3^2 & +iq\kappa_3 \\ 0 & +iq\kappa_3 & q^2 \end{pmatrix} - k_0^2 \hat{\varepsilon}_{b_0}(\omega, q), \quad (2.9)$$

with

$$\hat{\varepsilon}_{b_0}(\omega, q) = \begin{pmatrix} \varepsilon & -\frac{k_3 c}{\Omega_p} \varepsilon_{b_0} & +\frac{iqc}{\Omega_p} \varepsilon_{b_0} \\ +\frac{k_3 c}{\Omega_p} \varepsilon_{b_0} & \varepsilon & 0 \\ -\frac{iqc}{\Omega_p} \varepsilon_{b_0} & 0 & \varepsilon \end{pmatrix}. \quad (2.10)$$

In spite of two former cases, in this case the dielectric tensor has a direct dependence on the propagation wave

vector \mathbf{q} . The diagonal terms of the dielectric tensors in Eqs. 2.6, 2.8 and 2.10 are equal to $\varepsilon(\omega) = \varepsilon_\infty(1 - \frac{\Omega_p^2}{\omega^2})$ and off diagonal terms are determined by $\varepsilon_b(\omega) = \varepsilon_\infty \frac{\omega_b}{\omega}$ and $\varepsilon_{b_0}(\omega) = \varepsilon_\infty \frac{\omega_{b_0}^2}{\omega^2}$. Here $\Omega_p^2 = \frac{4\alpha}{3\pi} (\frac{\mu}{\hbar})^2$ refers to the bulk plasmon frequency with $\alpha = \frac{e^2}{\hbar v_f \varepsilon_\infty}$, $\omega_b = 2e^2 |b| / \pi \hbar \varepsilon_\infty$, $\omega_{b_0}^2 = \frac{2e^2 b_0 \Omega_p}{\pi \hbar c \varepsilon_\infty}$ and $k_0 = \frac{\omega}{c}$ is the wave vector in the vacuum. It should be noticed that we have ignored the effect of the carrier scattering in the dielectric tensor of WSMs due to the very low carrier scattering rates measured in this class of materials^{9,11}.

Setting the determinant of \hat{M} matrices in Eqs. 2.5, 2.7 and 2.9 to zero, the decay constant κ for aforementioned three different configurations are obtained. For the Voigt configuration the decay constant should be a positive and real number and is obtained as,

$$\kappa_{v+}^2 = q^2 - k_0^2 \varepsilon, \quad \kappa_{v-}^2 = q^2 - k_0^2 \varepsilon_v, \quad (2.11)$$

where $\varepsilon_v = (\varepsilon^2 - \varepsilon_b^2) / \varepsilon$ is the Voigt dielectric function. For the Faraday configuration it reads,

$$\kappa_{f\pm}^2 = q^2 - k_0^2 \varepsilon + k_0^2 \left(\frac{\varepsilon_b^2}{2\varepsilon} \right) \pm \left[k_0^4 \frac{\varepsilon_b^4}{4\varepsilon^2} + q^2 k_0^2 \frac{\varepsilon_b^2}{\varepsilon} \right]^{1/2}, \quad (2.12)$$

and for the case of $b_0 \neq 0$ is given by,

$$\kappa_{b_0\pm}^2 = q^2 - k_0^2 \varepsilon - \frac{1}{2} k_0^4 \varepsilon_{b_0}^2 \left(\frac{c}{\Omega_p} \right)^2 \pm \frac{1}{2} [k_0^8 \varepsilon_{b_0}^4 \left(\frac{c}{\Omega_p} \right)^4 + 4\varepsilon k_0^6 \varepsilon_{b_0}^2 \left(\frac{c}{\Omega_p} \right)^2]^{1/2}. \quad (2.13)$$

In the dielectric layer which is an isotropic medium the dielectric tensor is diagonal with elements equal to constant quantity ε_a . In this medium the decay constant is specified by $\kappa_2 = \sqrt{q^2 - k_0^2 \varepsilon_a}$.

SPP modes in the Voigt configuration: First, we consider the slot waveguide with Voigt configuration in the upper interface. The electric field amplitude in three mediums can be written as combination of the terms in the form of Eq. 2.2 with the appropriate decay constants in the related mediums²⁹. Applying the continuity condition for tangential components of the electric field, denoted by vector \hat{E}_t , we arrive at the following set of linear equations at the upper interface ($z = a/2$),

$$\begin{pmatrix} 1 & 0 & -e^{\kappa_2 a/2} & 0 & -e^{-\kappa_2 a/2} & 0 & 0 & 0 \\ 0 & 1 & 0 & -e^{\kappa_2 a/2} & 0 & -e^{-\kappa_2 a/2} & 0 & 0 \\ 0 & -\frac{\varepsilon_1 A}{\kappa_{v-}} \kappa_2 & 0 & -\varepsilon_0 e^{\kappa_2 a/2} & 0 & \varepsilon_0 e^{-\kappa_2 a/2} & 0 & 0 \\ -\kappa_{v+} & 0 & -\kappa_2 e^{\kappa_2 a/2} & 0 & \kappa_2 e^{-\kappa_2 a/2} & 0 & 0 & 0 \end{pmatrix} \hat{E}_t = 0, \quad (2.14)$$

and for the lower interface ($z = -a/2$) it reads,

$$\begin{pmatrix} 0 & 0 & -e^{-\kappa_2 a/2} & 0 & -e^{\kappa_2 a/2} & 0 & 1 & 1 \\ 0 & 0 & 0 & -e^{-\kappa_2 a/2} & 0 & -e^{\kappa_2 a/2} & \chi_1 & \chi_2 \\ 0 & 0 & 0 & -\varepsilon_0 k_0^2 e^{-\kappa_2 a/2} & 0 & \varepsilon_0 k_0^2 e^{\kappa_2 a/2} & \kappa_2 A_1 & \kappa_2 A_2 \\ 0 & 0 & -\kappa_2 e^{-\kappa_2 a/2} & 0 & \kappa_2 e^{\kappa_2 a/2} & 0 & \kappa_{b_0+} & \kappa_{b_0-} \end{pmatrix} \hat{E}_t = 0, \quad (2.15)$$

where $\varepsilon_{1A} = -\kappa_{v-}(iq\beta_1 + \kappa_{v-})$, $A_{1,2} = (iq\theta_{1,2} - \kappa_{b_0\pm}\chi_{1,2})$ with $\beta_1 = (iq\kappa_{v-} - k_0^2\varepsilon_b)/(q^2 - k_0^2\varepsilon)$, $\theta_{1,2} = [(-iq\kappa_{b_0\pm})(k_0^2c\varepsilon_{b_0}\kappa_{b_0\pm}/\Omega_p) - (iqk_0^2c\varepsilon_{b_0}/\Omega_p)(-\kappa_{b_0\pm}^2 - k_0^2\varepsilon)]/R$, $\chi_{1,2} = [(iq\kappa_{b_0\pm})(iqk_0^2c\varepsilon_{b_0}/\Omega_p) - (-k_0^2c\varepsilon_{b_0}\kappa_{b_0\pm}/\Omega_p)(q^2 - k_0^2\varepsilon)]/R$ and $R = (q^2 - k_0^2\varepsilon)(-\kappa_{b_0\pm}^2 - k_0^2\varepsilon) - (iq\kappa_{b_0\pm})^2$.

The SPP dispersion relation is obtained by setting the determinant of the coefficient matrix of Eqs. 2.14 and 2.15, which is a 8×8 matrix, to zero. The resultant dispersion relation is a lengthy equation, not presented here, which we solve it numerically to obtain SPP dispersion. But, we can find a very simplified expression for SPP dispersion relation in the nonretarded limit (long wavelength limit), $q \gg k_0$. In this limit all of the decaying constants tend to the same value of q , i.e. $\kappa_{b_0\pm} = \kappa_{v\pm} = \kappa_2 = q$. Applying these simplifications in Eqs. 2.14 and 2.15, lead to $\varepsilon_{1A} = (\varepsilon - \varepsilon_b)$, $\chi_1 = \chi_2 = 0$ and $A_1 = A_2 = 0$. Finally, by equating the determinant of the coefficient matrix of these simplified equations to zero, we can obtain SPP dispersion relation in the nonretarded limit,

$$\varepsilon[\varepsilon - \varepsilon_b + \varepsilon_d \tanh(aq)] = 0. \quad (2.16)$$

This relation reveals the chiral nature of the SPP propagation in the considered structure. Dependence of the dispersion relation to the sign of the propagation wave vector (q) results in different SPP dispersion for the forward and backward directions. The asymptotic frequencies for SPP dispersion, frequencies of SPP modes at the long wavelength limit $|q| \rightarrow \infty$, are obtained by taking the limit of $a|q| \gg 1$ in Eq. 2.16. This leads to equations $\varepsilon - \varepsilon_b + \varepsilon_d = 0$ and $\varepsilon = 0$, giving the asymptotic frequencies as,

$$\begin{aligned} \omega_{as}^{v\pm} &= \frac{\sqrt{\varepsilon_\infty^2 \omega_b^2 + 4\varepsilon_\infty \Omega_p^2 (\varepsilon_d + \varepsilon_\infty) \pm \varepsilon_\infty \omega_b}}{2(\varepsilon_d + \varepsilon_\infty)}, \\ \omega_{as}^{b_0} &= \Omega_p. \end{aligned} \quad (2.17)$$

SPP modes in the Faraday configuration: Employing the same procedure explained for Voigt configuration, we can obtain the following set of linear equations for tangential electric filed amplitudes at the upper interface ($z = +a/2$),

$$\begin{pmatrix} 1 & 1 & -e^{\kappa_2 a/2} & 0 & -e^{-\kappa_2 a/2} & 0 & 0 & 0 \\ -qA_+\kappa_{f+} & -qA_-\kappa_{f-} & 0 & -\alpha e^{\kappa_2 a/2} & 0 & -\alpha e^{-\kappa_2 a/2} & 0 & 0 \\ \eta A_+ & \eta A_- & 0 & -\beta e^{\kappa_2 a/2} & 0 & \beta e^{-\kappa_2 a/2} & 0 & 0 \\ -\kappa_{f+} & -\kappa_{f-} & -\kappa_2 e^{\kappa_2 a/2} & 0 & \kappa_2 e^{-\kappa_2 a/2} & 0 & 0 & 0 \end{pmatrix} \hat{E}_t = 0, \quad (2.18)$$

and at the lower interface ($z = -a/2$) we have,

$$\begin{pmatrix} 0 & 0 & -e^{-\kappa_2 a/2} & 0 & -e^{\kappa_2 a/2} & 0 & 1 & 1 \\ 0 & 0 & 0 & -e^{-\kappa_2 a/2} & 0 & -e^{\kappa_2 a/2} & \chi_1 & \chi_2 \\ 0 & 0 & 0 & -\beta e^{-\kappa_2 a/2} & 0 & \beta e^{\kappa_2 a/2} & \kappa_2 B_1 & \kappa_2 B_2 \\ 0 & 0 & -\kappa_2 e^{-\kappa_2 a/2} & 0 & \kappa_2 e^{\kappa_2 a/2} & 0 & \kappa_{b_0+} & \kappa_{b_0-} \end{pmatrix} \hat{E}_t = 0, \quad (2.19)$$

where $\beta = k_0^2\varepsilon_d$, $\alpha = k_0^2\varepsilon_b$, $A_\pm = \frac{q^2 - \kappa_{f\pm}^2 - k_0^2\varepsilon}{\kappa_{f\pm}^2 + k_0^2\varepsilon}$, $\eta = \frac{q\kappa_2\varepsilon}{k_0^2\varepsilon_d\varepsilon_b}$, $B_{1,2} = iq\theta_{1,2} - \kappa_{b_0\pm}\chi_{1,2}$ with $\theta_{1,2}$ and $\chi_{1,2}$ as defined earlier. Setting the determinant of the coefficient matrix of Eqs. 2.18 and 2.19 to zero, once again gives rise to a lengthy equation for dispersion relation of the Faraday configuration. In this case, dispersion relation does not depend on the sign of q and thus the resultant SPP modes should be reciprocal. In the nonretarded limit, $q \gg k_0$, we have $A_{f\pm} = 0$, $B_{1,2} = 0$, $\kappa_{b_0\pm} = \kappa_{f\pm} = \kappa_2 = q$ and the dispersion relation reduces to,

$$\varepsilon[\varepsilon + \varepsilon_d \tanh(a|q|)] = 0, \quad (2.20)$$

Again, by taking the long wavelength limit $a|q| \gg 1$, we get the equations $\varepsilon = 0$ and $\varepsilon + \varepsilon_d = 0$, which lead to the asymptotic frequencies for Faraday configuration as,

otic frequencies for Faraday configuration as,

$$\begin{aligned} \omega_{as}^f &= \Omega_p \sqrt{\frac{\varepsilon_\infty}{\varepsilon_\infty + \varepsilon_d}}, \\ \omega_{as}^{b_0} &= \Omega_p. \end{aligned} \quad (2.21)$$

In the next section we present our numerical results for the SPP dispersion for both Voigt and Faraday configurations. We will show that topological properties pave as a feasible way for stable tuning of SPP propagation without need for application of an external magnetic field.

III. RESULTS AND DISCUSSION

Numerical solution of the dispersion relations give dispersion curves for SPP modes in the slot waveguide with

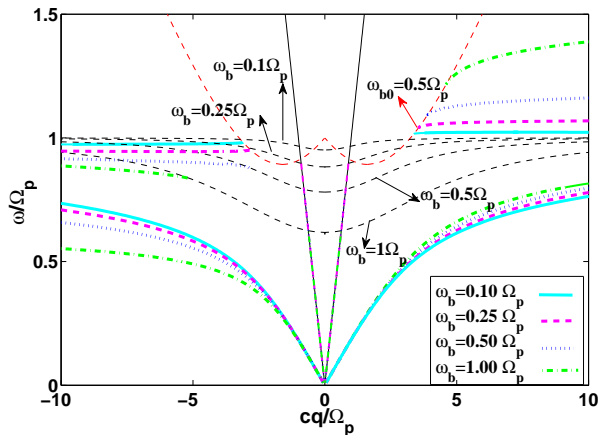


FIG. 2: SPP dispersion of the slot waveguide in Voigt configuration at the upper interface with $\varepsilon_\infty = 13$, $E_f = 0.15$ eV, $v_f = 10^6$ m/s, $\Omega_p = 60.92$ THz, $\varepsilon_d = 1.0$ and for $\omega_{b0} = 0.5 \Omega_p$, $\omega_b = 0.1, 0.25, 0.5, 1.0 \Omega_p$. The bulk plasmon dispersions related to the upper WSM in Voigt configuration are indicated by the thin black dash lines and that for WSM with broken SIS ($b_0 \neq 0$) is shown by the thin red dash line.

Voigt and Faraday configurations. In numerical calculation we adopt the measured parameters for $Eu_2Ir_2O_7$ as a typical parameters for a WSM: $\varepsilon_\infty = 13$, $E_f = 0.15$ eV, $v_f = 10^6$ m/s, $\Omega_p = 60.92$ THz, which have been used in several studies^{26–29}.

The slot waveguide with Voigt configuration: First we consider the case of Voigt configuration at the upper interface. In Fig. 2 we have exhibited the SPP dispersion in Voigt configuration for both $q > 0$ and $q < 0$ for different values of $\omega_b = 0.1, 0.25, 0.5, 1.0 \Omega_p$ and $\omega_{b0} = 0.5 \Omega_p$. As it is expected from the dispersion relation (Eq. 2.16) the SPP dispersion is nonreciprocal in this case and depends on the propagation direction. There are higher and lower SPP dispersion bands for both $q > 0$ and $q < 0$. In addition, there exist a reciprocal SPP dispersion band lying on the light line corresponding to the lower WSM with broken SIS. The lower SPP dispersion curves start from the zero frequency and continuously tend to their asymptotic frequency given by ω_{as}^- in Eq. 2.17. The higher SPP dispersion curves terminate when intersect with the bulk plasmon modes which have been indicated by the black thin dash lines and red thin dash line for the upper and lower WSMs, respectively. These dispersion curves approach to their asymptotic frequencies given by ω_{as}^+ in Eq. 2.17 for $q > 0$ and $\omega_{as}^{b_0}$ for $q < 0$. The asymptotic frequencies depend on the physical parameters of WSMs such as Weyl nodes separation vector (\mathbf{b}) and chemical potential (μ). Thus, it is obvious that we can tune the SPP modes by changing the WSMs parameters. The dispersion curves lying on the light line start from the zero frequency and end when coincide with bulk plasmon modes belonging to the lower WSM. It is remarkable that the SPP modes with frequencies below the Ω_p are nonreciprocal but propagate bidirectional while the SPP modes with frequencies above the bulk plasmon frequency are chiral and propagate unidirectional. This fascinating result is in contrast with the SPP modes hosted by a single interface of a WSM and a dielectric in Voigt configuration²⁶. The later structure supports SPP modes for $q < 0$ with frequencies

above the bulk plasmon frequency, while these modes disappear in the waveguide structure due to their propagation in the bulk of the lower WSM with broken SIS. This is a striking result which shows a profound tunability of SPP modes in the waveguide structure by involving second WSM with broken SIS. By increasing ω_b dispersion curves for $q > 0$ shift toward higher frequencies. This shift is more significant for curves above the bulk plasmon frequency. For $q < 0$ the dispersion curves show an inverse behavior and their frequencies decrease by increasing ω_b .

The normalized intensity of y component of the electric field for lower and higher bands of SPP dispersion have been depicted respectively in Figs. 3 (a) and (b) as a function of z position. The profile of the electric field for $\omega_b = 0.1 \Omega_p$ (at frequencies 46.42 THz for $q > 0$ and 44.69 THz for $q < 0$) and $\omega_b = 1.0 \Omega_p$ (at frequencies 49.70 THz for $q > 0$ and 33.62 THz for $q < 0$) are indicated by solid and dash lines, respectively. The electric field profile in Figs. 3 (a) and (b) reveal that the SPP modes related to positive wave number, the black lines, for lower (higher) band is mostly localized at the lower (higher) interface while the SPP modes with negative wave number, the red lines, have inverse behavior. A remarkable feature is that the SPP modes become highly confined to the corresponding interfaces by increasing ω_b .

Decay constants for SPP modes of the bands with frequencies below the bulk plasmon frequency are pure real and positive in the upper WSM with Voigt configuration ($\kappa_{v\pm}$) which ensures decaying of the electric field away from the interface while those for the lower WSM with broken SIS ($\kappa_{b_0\pm}$) are complex conjugates of each other which provide the electric field to oscillatory decay into the lower WSM. Therefore, these SPP modes are categorized as generalized surface waves²⁹. On the other hand, decay constants for SPP modes having frequencies above the bulk plasmon frequency (only exist for $q > 0$) are real and positive, which these SPP modes are known as normal surface waves. To illustrate dependence of the decaying constants on wave vector, we have plotted the real and imaginary parts of the reduced decay constants $\beta_{v-} = \kappa_{v-}/q$ and $\beta_{b_0-} = \kappa_{b_0-}/q$ as a function of q for lower and higher bands of SPP dispersion for $q > 0$ in Figs. 4 (a) and (b), respectively. For lower band, Fig. 4 (a), β_{v-} is real, while β_{b_0-} is complex with an imaginary part approaching to zero in the limit of large wave vectors. But, both of these decaying constants are real and positive for SPP modes of the upper band (Fig. 4 (b)) and tend to a same constant value ($\beta = 1$) at large wave vectors.

Moreover, the localization length ($\lambda_{li} = 1/Re(\kappa)$) normalized to the waveguide width (a) have been plotted against wave vector in Fig. 5 for higher and lower SPP bands for different ω_b . By decreasing ω_b , the localization length in the upper WSM (κ_{v-}) for lower (higher) SPP band decreases (increases), while the localization length in the lower WSM for lower (higher) SPP band remain intact (decreases) at small wave vectors. All of λ_{li} for both the higher and lower bands approach to $\lambda_{li} = 2a$ at large wave vectors.

To study dependence of the SPP dispersion on the parameters of the lower WSM we have plotted them as a function of wave vector for different $\omega_{b0} = 0.1, 0.25, 0.5, 0.75 \Omega_p$ and $\omega_b = 0.5 \Omega_p$ for $a = 0.1 \mu\text{m}$ in Fig. 6. As we can see, there is no significant variation in SPP dispersion by changing ω_{b0} , except small variations in the short wave vectors close to the bulk plasmon dispersion curves. These variations take place due to the change in the bulk plasmon dispersion by changing ω_{b0} . In Figs. 7 (a) and (b) the normalized localization

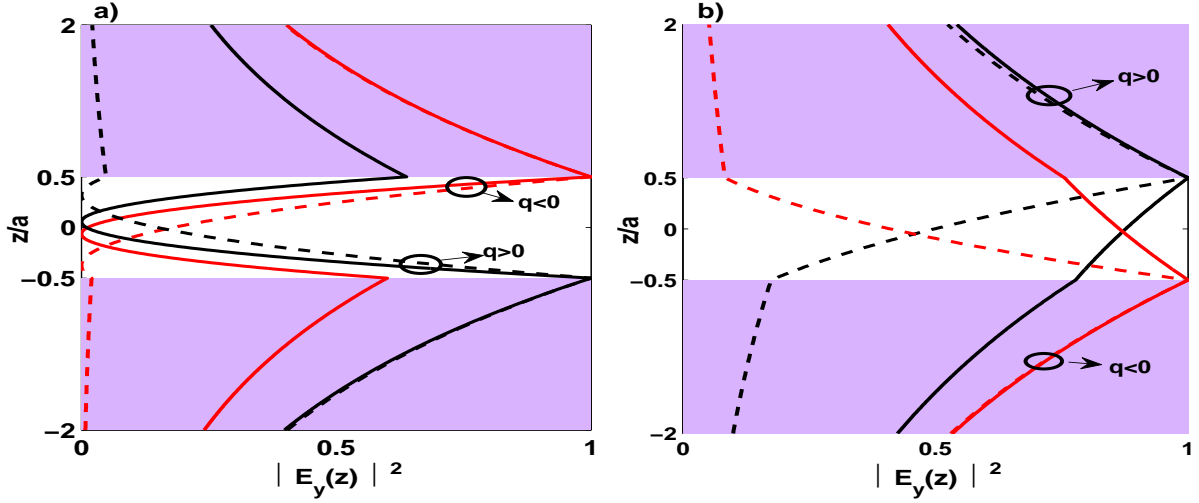


FIG. 3: The normalized electric field intensity of SPP modes of a) lower and b) higher bands as a function of z coordinate for the waveguide width $a = 0.1 \mu m$ and different $\omega_b = 0.1, 1.0 \Omega_p$ that have been shown by solid and dash lines, respectively. The other parameters are same as Fig. 2. The black lines denote the electric field profile for positive wave number ($q > 0$) and the red ones for negative wave number ($q < 0$).

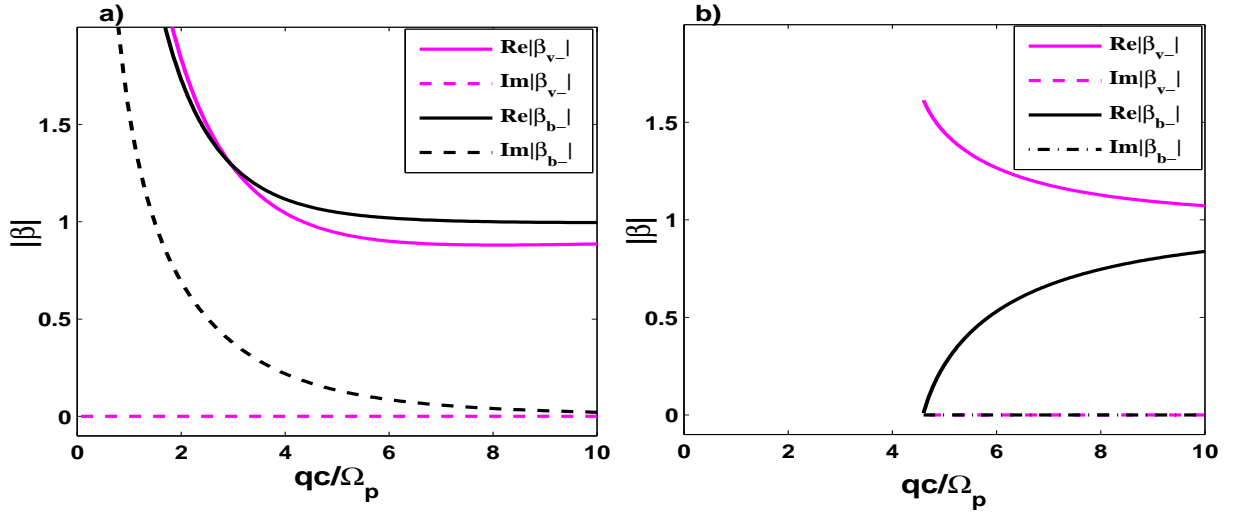


FIG. 4: Real and imaginary parts of the reduced decay constants of SPP modes for a) lower and b) higher bands for $q > 0$ as a function of q shown respectively by solid and dash lines with $a = 0.1 \mu m$, $\omega_b = 1 \Omega_p$ and $\omega_{b_0} = 0.5 \Omega_p$.

length (λ_U/a) is plotted for the lower and higher SPP bands with different ω_{b_0} . As it is apparent from these figures, in spite of the negligible variation in the SPP modes frequency with changing ω_{b_0} , there is a significant change in the reduced decay constant of the lower WSM. It decreases for all wave vectors by decreasing ω_{b_0} .

Dependence of the SPP dispersion on the dielectric constant of the dielectric layer has been shown in Fig. 8, which we have plotted SPP dispersion for $\epsilon_d = 1.0, 2.0, 3.0$ with $\omega_b = \omega_{b_0} = 0.25 \Omega_p$ and $a = 0.1 \mu m$. By increasing ϵ_d a substantial decrease is seen in the lower bands and the bands lying on the light line while the higher bands remain almost

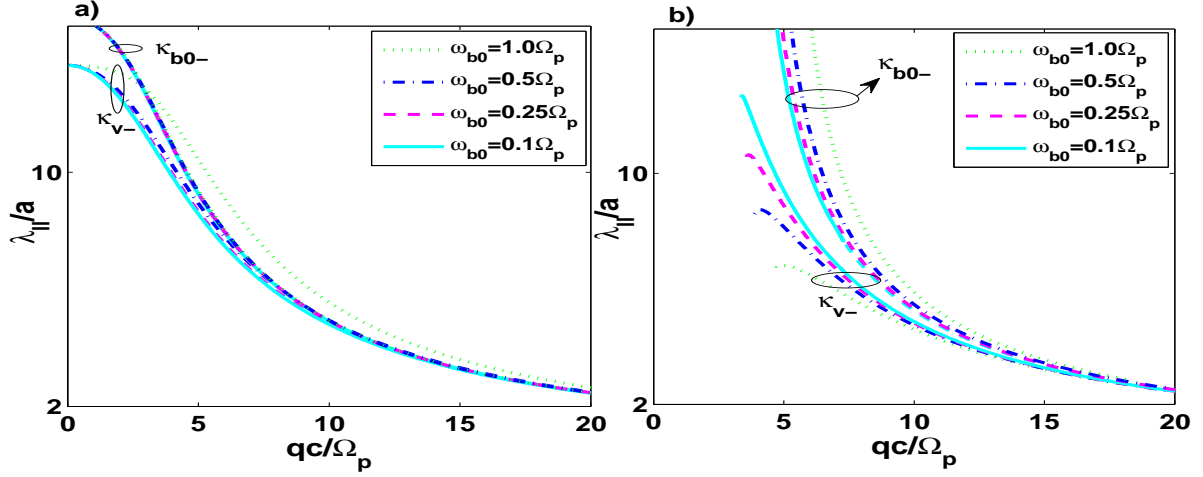


FIG. 5: The normalized localization length versus SPP wave vector for a) lower and b) higher SPP bands with $a = 0.1 \mu\text{m}$, $\omega_{b0} = 0.5 \Omega_p$ and for different $\omega_b = 0.1, 0.25, 0.5, 1 \Omega_p$.

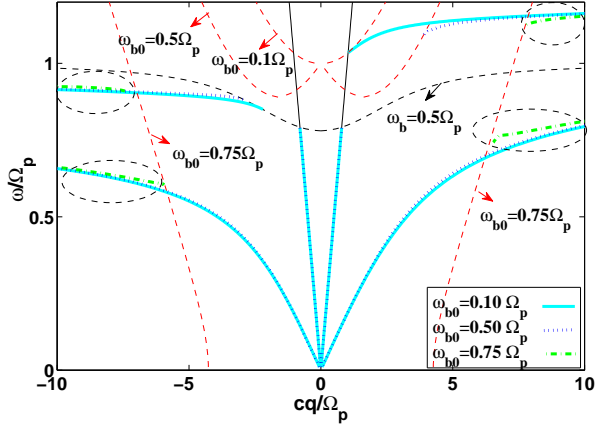


FIG. 6: SPP dispersion of the slot waveguide in Voigt configuration at the upper interface for $\omega_b = 0.5 \Omega_p$, different $\omega_{b0} = 0.1, 0.5, 0.75 \Omega_p$ and the other parameters same as Fig. 2. The bulk plasmon dispersions related to the upper WSM in Voigt configuration and the lower WSM with broken SIS ($b_0 \neq 0$) are denoted by the thin red dash line and thin black dash line, respectively.

intact.

The slot waveguide with Faraday configuration: Now we turn to study SPP dispersion of a slot waveguide with Faraday configuration at the upper interface. Since, the resultant dispersion curves are reciprocal, thus we show dispersion curves only for $q > 0$. Fig. 9 shows SPP dispersion for waveguide widths $a = 0.1, 1.0 \mu\text{m}$ and the other parameters same as

Fig. 2. In this case there are two bands both below the bulk plasmon frequency. The lower band starts from the origin and then approaches to the asymptotic frequency ω_{as}^f given by Eq. 2.21, but the higher band is comprised of two branches with a gap between them. The lower branch rises just to the right of the light line and terminates when it intersects the bulk plasmon dispersion while the higher branch is a nearly flat band which starts at the bulk plasmon frequency and finally tends to its asymptotic frequency $\omega_{as}^b = \Omega_p$. In Figs. 9 (a)-(d) we have compared dispersion curves for different waveguide widths and different values of ω_b . As we can see from the figures, decreasing the waveguide width leads to shift of the lower band to the lower frequencies and increment of the gap of the higher band. Although, increasing ω_b does not alter the lower band but it leads to enlarging the gap of the higher band.

In Figs. 10 (a) and (b) the normalized y component of the electric field intensity has been shown for two different values of $\omega_b = 1.0, 0.25 \Omega_p$ at asymptotic frequencies for both higher and lower bands with waveguide widths $a = 0.1 \mu\text{m}$ and $a = 1.0 \mu\text{m}$ denoted respectively by the solid and the dash-dot lines. As we can see, in both figures the electric field profile is nearly symmetric with respect to the z coordinate for a small waveguide width ($a = 0.1 \mu\text{m}$ denoted by solid lines), while it is asymmetric for a large waveguide width ($a = 1.0 \mu\text{m}$ denoted by dash-dot lines). The symmetric profile for the electric field arises from the effective mixing of the SPP modes at two upper and lower interfaces in small waveguide widths. However, in the limit of a wide waveguide this hybridization is not considerable and SPP modes belonging to lower (higher) band are highly localized at the upper (lower) interface. The electric field intensity is suppressed to zero at the middle of the dielectric layer for $\omega_b = 1.0 \Omega_p$ (Fig. 10 (a)) and for $\omega_b = 0.25 \Omega_p$ (Fig. 10 (b)) except the SPP modes of the

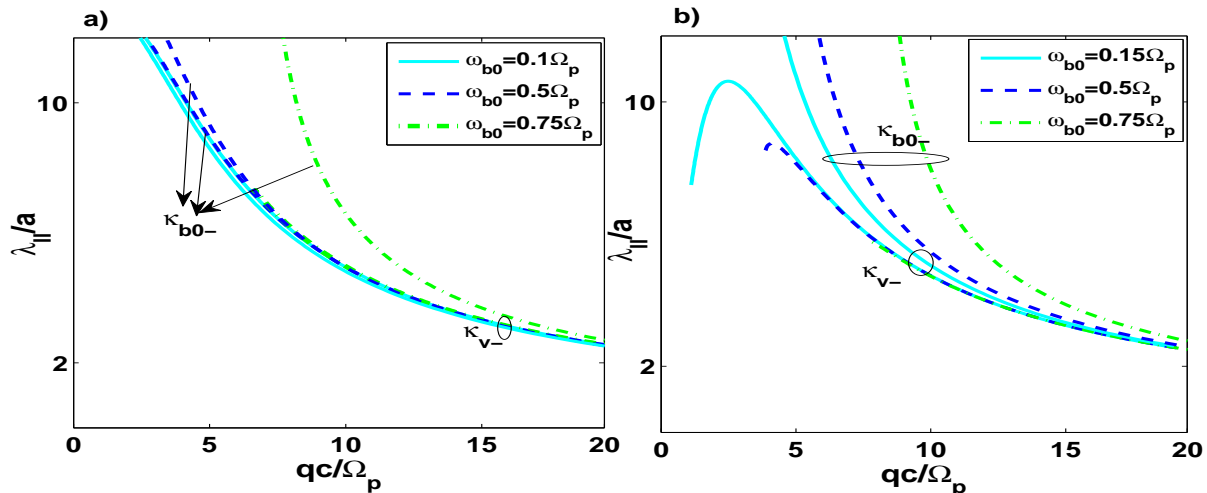


FIG. 7: The normalized localization length versus SPP wave vector for a) lower and b) higher bands of the slot waveguide in Voigt configuration at the upper interface with $a = 0.1 \mu\text{m}$, $\omega_b = 0.5 \Omega_p$ and different $\omega_{b0} = 0.1, 0.5, 0.75 \Omega_p$.

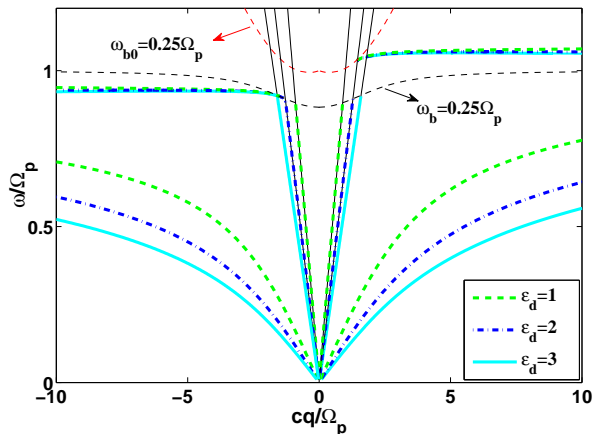


FIG. 8: Surface plasmon polariton dispersion of the slot waveguide in Voigt configuration at the upper interface for $\omega_b = \omega_{b0} = 0.25 \Omega_p$ and for different dielectric constants of the dielectric layer $\varepsilon_d = 1.0, 2.0, 3$.

higher band for small waveguide widths.

The decay constants in both upper and lower WSM media have complex values for SPP modes of both higher and lower bands. The real parts of them tend to q , but their imaginary parts approaches to zero for large wave vectors. So, it is clear that the real parts of decay constants are more dominant than their imaginary parts at large wave vectors while both of them play significant rule at small wave vectors. For example, Fig. 11 (a) shows real and imaginary parts of the reduced decay constants $\beta_{f-} = \kappa_{f-}/q$ and $\beta_{b0-} = \kappa_{b0-}/q$ of lower band for

$a = 0.1 \mu\text{m}$. Moreover, localization length in the upper and lower WSMs and for both SPP modes of higher and lower bands decay with respect to q and approaches to $2a$ at the limit of the large wave vectors. We have shown $\lambda_{||}/a$ in Fig. 11 (b) as a function of qc/Ω_p for both higher and lower bands for $a = 0.1 \mu\text{m}$, $\omega_b = 0.1 \Omega_p$ and $\omega_{b0} = 0.5 \Omega_p$.

IV. CONCLUSION

In summary we have investigated the dispersion, the electric field profile and the localization length of SPP modes hosted by a WSM waveguide constructed by two WSMs with distinct symmetries. We found that incorporating a WSM with broken SIS drastically modifies the SPP modes corresponding to a single interface of a WSM with broken TRS in both Voigt and Faraday configurations. In the Voigt configuration inclusion of the second WSM leads to a giant unidirectional SPP modes in the frequencies above the bulk plasmon frequency. The SPP modes supported by the waveguide structure in the Faraday configuration are comprised of two bands including a gapfull and one gapless band. Our investigations revealed that the SPP modes dispersion and localization can be effectively tuned by the waveguide characteristic parameters such as the topological properties of two WSMs. The anomalous Hall effect and chiral magnetic effect which depend on the separation of the Weyl nodes in momentum space and energy determine the strength of the coupling of the electrical and magnetical properties of WSMs. The inhomogeneous optical response of WSMs originating from transverse or Hall conductivity of these materials is estimated to be several orders of magnitude larger than typical magnetic dielectrics^{27,28}. Therefore, a stable and efficient control of

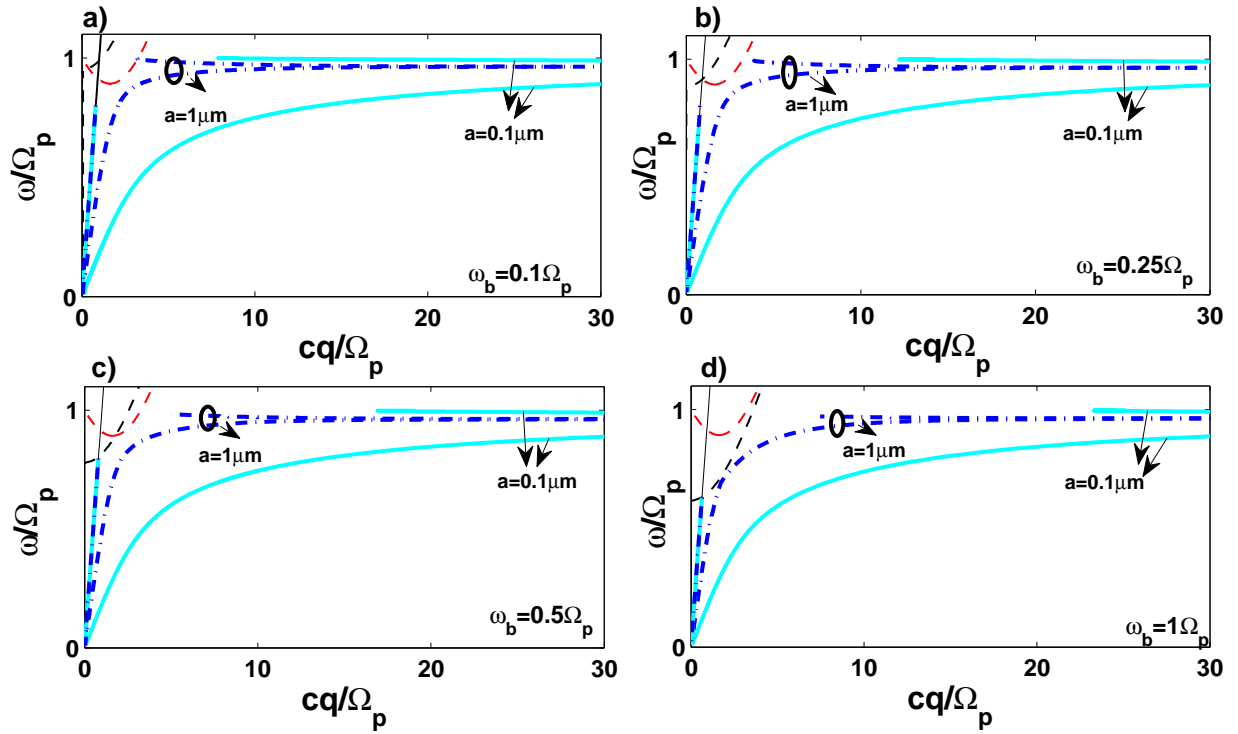


FIG. 9: SPP dispersion of the slot waveguide in Faraday configuration at the upper interface for waveguide widths $a = 0.1, 1.0 \mu\text{m}$, $\omega_{b_0} = 0.5 \Omega_p$ and for different $\omega_b = 0.1, 0.25, 0.5, 1.0 \Omega_p$. The other parameters are same as Fig. 2 and the black and red dash lines denote the bulk plasmon dispersions.

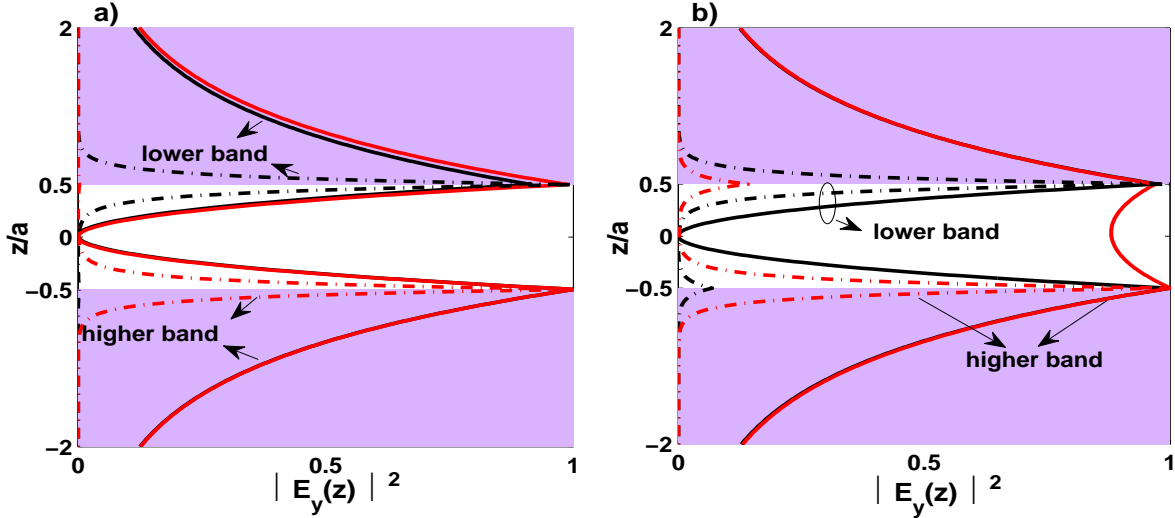


FIG. 10: The normalized electric field intensities of the slot waveguide in Faraday configuration at the upper interface by assuming $\omega_{b_0} = 0.5 \Omega_p$ and for a) $\omega_b = 1.0 \Omega_p$ and b) $\omega_b = 0.25 \Omega_p$ with $a = 1.0 \mu\text{m}$ and $a = 0.1 \mu\text{m}$ indicated by the dash-dot and solid lines, respectively. The red lines denote profile of the electric field for a SPP mode of the higher band and the black ones are for the lower band.

SPP propagation at the interface of WSMs can be achieved by their intrinsic topological properties. Practically, the chi-

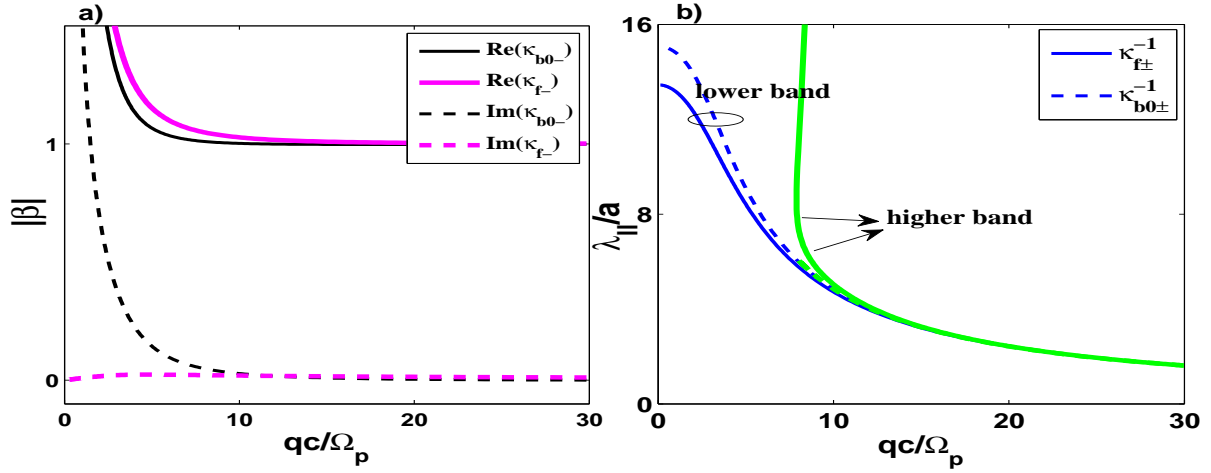


FIG. 11: a) Real and imaginary parts of the reduced decay constants versus wave vector for lower band with $\omega_{b_0} = 0.5 \Omega_p$, $\omega_b = 0.1 \Omega_p$ and $a = 0.1 \mu m$. b) The normalized localization length as a function of the wave vector for both lower and higher bands with $\omega_{b_0} = 0.5 \Omega_p$, $\omega_b = 0.1 \Omega_p$ and $a = 0.1, 1.0 \mu m$.

ral quantum optics which deals with propagation-direction-dependent light-matter interactions has attracted great attention recently⁴³. The chiral SPP modes reported here may be

employed in developing unidirectional optical circuits⁴⁴ and the directed excitations in a ring lasers⁴⁵.

-
- ¹ Armitage N P, Mele E J and Vishwanath A 2018 Rev. Mod. Phys. **90** 015001
 - ² Murakami S 2007 New J. Phys. **9** 356
 - ³ Wan X, Turner A M, Vishwanath A and Savrasov S Y 2011 Phys. Rev. B **83** 205101
 - ⁴ Fang Z, Nagaosa N, Takahashi K S, Asamitsu A, Mathieu R, Ogasawara T, Yamada H, Kawasaki M, Tokura Y and Terakura K 2003 Science **302** 92
 - ⁵ Burkov A A and Balents L 2011 Phys. Rev. Lett. **107** 127205
 - ⁶ Halasz G B and Balents L 2012 Phys. Rev. B **85** 035103
 - ⁷ Xu S Y, Belopolski I, Alidoust N, Neupane M, Bian G, Zhang C, Sankar R, Chang G, Yuan Z, Lee C C, Huang S M, Zheng H, Ma J, Sanchez D S, Wang B, Bansil A, Chou F, Shibaev P P, Lin H, Jia S, and Hasan M Z 2015 Science **349**, 613
 - ⁸ Xu S Y, Alidoust N, Belopolski I, Yuan Z, Bian G, Chang T R, Zheng H, Strocov V N, Sanchez D S, Chang G, Zhang C, Mou D, Wu Y, Huang L, Lee C C, Huang S M, Wang B, Bansil A, Jeng H T, Neupert T, Kaminski A, Lin H, Jia S, and Zahid Hasan M 2015 Nat. Phys. **11**, 748
 - ⁹ Shekhar C, Nayak A K, Sun Y, Schmidt M, Nicklas M, Leermakers I, Zeitler U, Skourski Y, Wosnitzer J, Liu Z, Chen Y, Schnelle W, Borrmann H, Grin Y, Felser C and Yan B 2015 Nat. Phys. **11**, 645-650
 - ¹⁰ Wan X, Turner A M, Vishwanath A, and Savrasov S Y 2011 Phys. Rev. B **83** 205101
 - ¹¹ Sushkov A B, Hofmann J B, Jenkins G S, Ishikawa J, Nakatsuji S, Das Sarma S, and Drew H D 2015 Phys. Rev. B **92**, 241108
 - ¹² Wu Y, Mou D, Jo N H, Sun K, Huang L, Bud'ko S, P, Kaminski A 2016 Phys. Rev. B **94**, 121113(R)
 - ¹³ Jiang J, Liu Z K, Sun Y, Yang H F, Rajamathi C R, Qi Y P, Yang L X, Chen C, Peng H, Hwang C C, Sun S Z, Mo S K, Vobornik I, Fujii J, Parkin S S P, Felser C, Yan B H and Chen Y L 2017 Nature Commun. **8**, 13973
 - ¹⁴ Parameswaran S A, Grover T, Abanin D A, Pesin D A and Vishwanath A 2014 Phys. Rev. X **4** 031035
 - ¹⁵ Xu G, Weng H M, Wang Z J, Dai X and Fang Z 2011 Phys. Rev. Lett. **107** 186806
 - ¹⁶ Burkov A A 2014 Phys. Rev. Lett. **113** 187202
 - ¹⁷ Huang X, Zhao L, Long L, Wang P, Chen D, Yang Z, Liang H, Xue M, Weng H, Fang Z, Dai X and Chen G 2015 Phys. Rev. X **5** 031023
 - ¹⁸ Zyuzin A A and Burkov A A 2012 Phys. Rev. B **86** 115133
 - ¹⁹ Chen Y, Wu Si and Burkov A A 2013 Phys. Rev. B **88** 125105
 - ²⁰ Vazifeh M M and Franz M 2013 Phys. Rev. Lett. **111** 027201
 - ²¹ Ashby P E C, Carbotte J P 2013 Phys. Rev. B **87** 245131
 - ²² Ashby P E C and Carbotte J P 2014 Phys. Rev. B **89** 245121

- ²³ Halterman K, Alidoust M, and Zyuzin A 2018 Phys. Rev. B **98** 085109
- ²⁴ Zhou J, Chang H R, and Xiao D 2015 Phys. Rev. B **91** 035114
- ²⁵ Zyuzin A A and Zyuzin V A 2015 Phys. Rev. B **92** 115310
- ²⁶ Hofmann J and Das Sarma S 2016 Phys. Rev. B **93** 241402(R)
- ²⁷ Kotov O V and Lozovik Yu E 2018 Phys. Rev. B **98** 195446
- ²⁸ Tamaya T, Kato T, Tsuchikawa K, Konabe S and Kawabata S 2019 J. Phys.: Condens. Matter **31** 305001
- ²⁹ Oskoui Abdol S, Soltani Vala A, and Abdollahipour B 2019 J. Phys.: Condens. Matter **31** 335002
- ³⁰ Tan C, Yue Z, Dai Z, Bao Q, Wang X, Lu H and Wang L 2018 Opt. Mater. **86**, 421
- ³¹ Maier S A, Plasmonics: Fundamentals and Applications (Springer, Berlin, 2007).
- ³² Homola J, Yee S S and Gauglitz G 1999 Sens. Actuators B Chem. **54** 3
- ³³ Novotny L and Stranick S J 2006 Ann. Rev. Phys. Chem. **57** 303
- ³⁴ Kane C L and Mele E J 2005 Phys. Rev. Lett. **95** 146802
- ³⁵ Hasan M Z and Kane C L 2010 Rev. Mod. Phys. **82** 3045
- ³⁶ Raghu S, Chung S B, Qi X L, and Zhang S C 2010 Phys. Rev. Lett. **104**, 116401
- ³⁷ Efimkin D K, Lozovik Y E, and Sokolik A A 2012 Nanoscale Res. Lett. **7**, 163
- ³⁸ Karch A 2011 Phys. Rev. B **83**, 245432
- ³⁹ Schutky R, Ertler C, Trugler A, and Hohenester U 2013 Phys. Rev. B **88**, 195311
- ⁴⁰ Qi J, Liu H, and Xie X C 2014 Phys. Rev. B **89**, 155420
- ⁴¹ Di Pietro P, Ortolani M, Limaj O, Di Gaspere A, Giliberti V, Giorgianni F, Brahlek M, Bansal N, Koirala N, Oh S, Calvani P, and Lupi S 2013 Nat. Nanotechnol. **8**, 556
- ⁴² Lu H, Dai S, Yue Z, Fan Y, Cheng H, Di J, Mao D, Li E, Meia T and Zhao J 2019 Nanoscale **11**, 4759
- ⁴³ Lodahl P, Mahmoodian S, Stobbe S, Rauschenbeutel A, Schneeweiss P, Volz J, Pichler H and Zoller P 2017 Nature **541**, 473-480
- ⁴⁴ Dötsch H, Bahlmann N, Zhuromskyy O, Hammer M, Wilkens L, Gerhardt R, Hertel P and Popkov A F 2005 J. Opt. Soc. Am. B **22** 240
- ⁴⁵ Kravtsov N V and Kravtsov N N 1999 Quantum Electron. **29** 378